Microcellular Electrode Material for Microbial Bioelectrochemical Systems Synthesized by Hydrothermal Carbonization of Biomass derived precursors

Victoria Flexer[1,†,*], Nicolas Brun[2,*], Bogdan C. Donose[1], Camille Lefebvre[1], Guillermo Pozo-Zamora[1], Matthieu N. Boone[3], Luc Van Hoorebeke[3], Mohamed Baccour[2], Laurent Bonnet[4], Sylvie Calas-Etienne[4], Anne Galarneau[2], Magdalena M. Titirici[5]

[1]The University of Queensland, Advanced Water Management Centre, Level 4, Gehrmann Building (60), Brisbane, QLD 4072, Australia

[2]Institut Charles Gerhardt de Montpellier, UMR 5253, CNRS-ENSCM-UM, Université de Montpellier, CC 1701, Place Eugène Bataillon, 34095 Montpellier, France

[3]Centre for X-ray Tomography, Dept. Physics and Astronomy, Ghent University, Proeftuinstraat 86, B-9000 Gent, Belgium

[4]Laboratoire Charles Coulomb, UMR 5221, CNRS-UM, Université de Montpellier, CC 069, Place Eugène Bataillon, 34095 Montpellier, France

[5]Queen Mary University of London, School of Engineering and Materials Science, Mile End Road, E1 4NS, London, United Kingdom

*corresponding authors:

Dr Victoria Flexer, vflexer@unju.edu.ar, (+54) 9388 4155 240;

Dr Nicolas Brun, nicolas.Brun@enscm.fr, (+33)4 67 16 34 66

[†]Present address: Centro de Investigaciones y Transferencia- JUJUY-CONICET.

Av. Bolivia 1239, San Salvador de Jujuy, 4600, Argentina

ABSTRACT

A new monolithic carbonaceous material, 750-HMF-CarboHIPE is presented here. The new electrode has been tested as an anode material inside a microbial bioelectrochemical system. In a purposely designed continuous flow bioelectrochemical reactor, the new material showed high biocompatibilty, with a continuous biofilm development that remained bioelectrochemically active for over 5 months. A catalytic current of 1.56 mA cm^{-2} / 7.8 mA cm^{-3} (normalization by projected surface area and volumetric current) was reached. The current density was proportional to the flow rate. The new electrode material was synthesized using a high internal phase emulsion (HIPE) as a soft template to confine the polymerization and hydrothermal carbonization of two precursors derived from the cellulosic fraction of biomass and the bark of fruit trees: respectively, 5-hydroxymethylfurfural and phloroglucinol. All together, the sustainable synthetic route from biomass materials and the proposed application of oxidizing organic matter present in wastewater to produce electricity in a microbial fuel cell (MFC) close an interesting loop of prospective sustainable technology.

Keywords

Microbial Bioelectrochemical systems; microbial fuel cells; electrochemically active biofilm; electrode material; porous carbons

Introduction

Carbon-based materials can be used in a wide variety of applications, thanks to a relative low cost and inherent attractive properties, such as high surface area, chemical inertness, thermal stability and electrical conductivity, [1-5] Porous carbons have been applied as adsorbents,[6-9] electrodes,[1, 10-13] catalytic[5, 14] or electrocatalytic supports,[4, 15-18] or even as intrinsic electrocatalysts[19-22]. In particular, macroporous carbons, exhibiting pores diameters larger than 50 nm within an interconnected framework, are promising as they present many structural advantages.[4, 15-18] Macropores increase the accessibility of the bulk and the associated active surface (*i.e.* smaller pores, functional groups, immobilized or adsorbed catalysts), while improving the mass transport rate through the whole porous network. This fact is particularly important when the aimed application involves the immobilization of bulky catalysts, such as particles, proteins or bacteria, and when the application requires the use of monolithic supports and/or continuous flow set-ups. Therefore, hierarchical macroporous carbons have been recently employed for the design of enzyme-based electrodes for bioelectrocatalysis and biofuel cells. In particular, the design of biosourced emulsion-templated carbons was recently proposed by some of us.[18, 22] These novel foams, named carbo-HIPEs (HIPE for High Internal Phase Emulsion [23]), complied most of the requirements in terms of functionality, easy design and shaping, and sustainability, necessary for many environmentally friendly applications. Notably, such microcellular monoliths were successfully used as bioelectrodes for the enzymatic oxidation of glucose.[18] These preliminary results gave a glimpse of the potential usage of biosourced carbo-HIPEs as electrodes in biofuel cells.

The synthetic precursors for these materials 5-(hydroxymethyl)furfural (5-HMF, a saccharide derivative), and phloroglucinol, can be isolated from the cellulosic fraction of lignocellulosic biomass, and extracted from the bark of fruit trees, respectively. This avoids using resorcinol/formaldehyde precursors and divinylbenzene-based polymers, constituting a most interesting renewable synthetic pathway.

The biofuel cell technology can be seen as a versatile and sustainable alternative for electricity generation in some specific applications. Biofuel cells employ active bioentities (*i.e.* enzymes or

bacteria) to convert environmentally friendly biomass or biofuels into “green” electrical power. In microbial bioelectrochemical systems (BES), whole cells are used as biocatalysts to catalyse oxidation and reduction reactions.[24-30] Microbial fuel cells (MFCs) are the classical and pioneer example of bioelectrochemical systems, performing the double task of wastewater treatment and electricity generation. The organic matter present in wastewater becomes the fuel to be oxidized all the way from multicarbon compounds to CO_2. In addition, the possibility of synthesizing higher value products from CO_2 or short carbon compounds at the cathode of a BES was recently envisioned, and has become an interesting candidate technology for the sustainable production of fuels and chemicals.[28-33] The economic feasibility and prospective industrial application of these systems is highly dependent on performance improvement, particularly increased electrical currents.[34-38] Current production or generation is dependent on several variables, most notably, the starting microbial community, bioelectrochemical reactor design, the operating conditions, and electrode materials.[36] While the first three characteristics have been widely researched for more than a decade, until not long ago, commercially available carbonaceous materials [24, 39, 40] such as carbon felt, carbon cloth, carbon paper, graphite granules or rods, etc., were employed almost exclusively in the field. The search for new advanced electrode materials, purposely designed for microbial bioelectrochemical applications is relatively recent.[17, 34, 41-57] The classical and straight forward approach in research on prospective electrode materials aims at increasing the active surface area available for biofilm growth. On the other hand, another strategy aims at designing materials with specific properties that will improve the bacteria-electrode interaction, and especially the rate of electron transfer.[58]

It would be a great advantage if three-dimensional anodes and cathodes could be employed for the construction of bioelectrochemical systems. Contrary to rough electrode surfaces or dense fibrous material such as carbon felt or graphite plates or granules, we refer here to true three-dimensional electrodes, where all three geometric dimensions are of the same order of magnitude, and where bacteria will be able to grow in the interior of the three-dimensional structure. Ideally, three-dimensional materials should bear macropores at least in the tens of micrometre scale in order to allow for efficient mass transport. Multidirectional pores are desirable to maximise fluid flow towards and out of the pores.[4, 15] In addition to ensuring efficient mass transfer to and from the electrode

surface, the macroporosity will drastically increase the accessible surface area of the electrode and therefore the microbial loading. In turn, porosity below known bacterial dimensions (nanopores or below) will help ensure efficient bacterial attachment and might eventually increase the electrode transfer rate. Indeed, nanometric features will create more electrical contact points between the bacterial electron transfer entities (be it nanowires, membrane proteins or soluble shuttles) and the solid electrode surface.[17]

The incorporation of electrode materials prepared from biomass molecules following a sustainable synthetic route into microbial electrochemical devices is an attractive idea. Indeed, whether we aim at green electricity generation, waste water treatment, or bioelectrosynthesis from CO_2, we would like to ensure that the synthesis of the electrodes also follows a green route.

Here we report on a new prospective microbial electrode material (750-HMF-CarboHIPE) bearing a hierarchical porous structure synthesized by hydrothermal carbonisation of emulsion-templated macroporous carbons. Results show that our new material is highly biocompatible. Uniform and continuous biofilm development was achieved in the outside surface of the electrode as well as in the interior of the scaffold. Partial clogging of the pores was observed, suggesting that an increase in pore size is still needed. Despite this clogging, the bacteria were electrically connected to the electrode surface and the bioelectrocatalytic current was stable during five months of continuous operation.

Experimental section

Electrode synthesis

Materials. Dodecane, Tween® 80 [Polyoxyethylene (20) sorbitan monooleate], iron (III) chloride hexahydrate ($FeCl_3.6H_2O$) and 5-(hydroxymethyl)furfural (5-HMF) were purchased from Sigma-Aldrich. Phloroglucinol 99% anhydrous was purchased from Acros Organic.

In a typical synthesis, non-ionic surfactant Tween® 80 (1 mL) was added in an hydroalcoholic mixture of water (2.4 mL) and absolute ethanol (2.4 mL). Then, phloroglucinol (0.312 g) and 5-HMF (0.572 g; corresponding to 1 molar equivalent of phloroglucinol for 2 equivalents of 5-

(hydroxymethyl)furfural) were mixed into this solution. After a vigorous stirring for a few minutes, iron (III) chloride hexahydrate (0.1335 g), acting as a Lewis acid catalyst, was added. The solution turned quickly black, due to the production of soluble polymers generated by fast reaction between the phenolic and furan compounds. Promptly, the prepolymerised hydroalcoholic solution was put in a mortar and dodecane (23.2 mL, corresponding to an oil volume fraction of 0.8) was added drop-by-drop while emulsification was performed manually with a pestle. The as-synthesized viscous emulsion was then added in a glass inlet (30 mL volume) sealed in a Teflon lined autoclave (45 mL volume) and placed in a laboratory oven preheated to 130°C and left for 24 hours. The HTC-CarboHIPE was then removed from the autoclave, washed by Soxhlet extraction with ethanol during 24 hours and dried at 80 °C in an oven. The dried HTC-CarboHIPE was placed in a ceramic crucible in a carbonisation oven and heated to 750°C under an inert atmosphere (i.e. N_2/Flow: 10 mL min^{-1}). We firstly used a ramp to reach 750 °C at a speed of 3 °C / minutes and then we remained at the isothermal step for 4 h. The sample was then allowed to cool to ambient conditions and removed from the oven prior to further analysis. The as-synthesized cellular porous carbon was then named 750-HMF-CarboHIPE. Finally, materials were shaped in cylindrical monoliths (0.2 cm high; 1.26 cm diameter).

Bioelectrochemical experiments

The electrodes were tested in a membraneless home-made electrochemical reactor. The reactor was made of two Perspex pieces. The first one consisted of a cylindrical compartment, 1.16 cm diameter, 1.8cm high, ending in a 1mm wide step at the top that widens the diameter to 1.26 cm and is 2 mm high, were the working electrode sits. A stainless steel ring, with an electrical connexion to the outside ensures the electrical contact with the working electrode. This contact is in turn reinforced by conductive carbon paint, which is let to dry for 1 day. An epoxy resin was used to sealed the electrode against the border to avoid media filtering this way and to ensure that both the inoculum and the feed filter through the pores of the electrode. There is a lateral compartment for the reference electrode just below the working electrode. The counter electrode mesh sits in between two bored 1mm rubber sheets which avoid leakages through the counter electrode. The upper Perspex compartment consists of only one cylinder 1.26 cm wide and 2 cm high. The two pieces are screwed tightly together to avoid

leakages. The reactor has an inlet in the bottom and an outlet at the top that allows for operation in continuous mode. Pictures of the reactor are shown in Figure S1 in Supporting Information. A Ag/AgCl (saturated Cl^-) reference electrode (CH Instruments, USA) was used and all potentials reported here are referred to this electrode. A large area Ti mesh was used as a counter electrode. All experiments were performed in triplicate, *i.e.* three replicate reactors were inoculated and run independently.

The working electrode was pre-treated in a N_2 plasma to increase the electrode hydrophilicity and increase the amount of N functionalities, as previoulsy shown by XPS.[59] The plasma treatment was performed after setting the working electrode in the reactor with carbon paint and glue reinforcement and just before assembling the two pieces of the reactor.

All bioelectrochemical experiments were carried out under strictly anoxic conditions (all solutions were bubbled with N_2 gas for 30 minutes). The electrode was introduced in the bioelectrochemical reactor and a solution of M9 medium without acetate (see below) was pumped continuously at a pumping rate of 0.25 mL min^{-1}. After 4 hours of continuous pumping, the background signal for Cyclic voltammograms (CVs) was measured (6 cycles). After CVs, a chronoamperometry experiment was started at an applied potential of 0V. The background current was measured prior to inoculation for 36 hours. The reactor was then inoculated with a mixture of 50 mL anodic effluent of an acclimatized bioelectrochemical reactor in our laboratory at The University of Queensland,[60] and 50ml of M9 media. This inoculum was pumped at a pumping rate of 1 mL h^{-1}. Time 0 in the current vs. time curves corresponds to the start of the inoculation. The reactor was later fed continuously with M9 medium and 20 mM acetate. The pumping rate was varied several times during the experiment, as specified in the results section.

Cyclic voltammograms in the presence of 20 mM acetate (turnover conditions) were measured at day 100. 6 consecutive CVs were measured; the last three scans showed reproducible results. At the end of the chronoamperometry experiment, fresh media without acetate was pumped for 36 hours, after which 6 cyclic voltammograms in the absence of acetate (non-turnover conditions) were measured, the last four scans showed reproducible scans. All cyclic voltammograms were recorded at a scan rate of 0.1 mV s^{-1}.

A Biologic VSP multichannel potentiostat was used for all experiments. A constant potential of 0V was applied for the total duration of the experiment, and was always on except for short periods of time when adjustments were made to the pumping system (never longer than 1 hour). Current values were measured every 200 s. The medium used was a modified M9 medium with 20 mM sodium acetate as the electron donor, which contains 6 g/ L Na_2HPO_4, 3 g/L KH_2PO_4, 0.1 g/L NH_4Cl, 0.5 g/L NaCl, 0.1 g/ L $MgSO_4 \cdot 7H_2O$, 14.6 mg/ L $CaCl_2$, and 1 mL/L of a mixed trace element solution as described in Rabaey *et al*.[61]

Experiments were run at room temperature (20 ± 3)^{o}C. The reported current values have been normalized by the projected surface area of the electrode (footprint). The reactor and all the pumping system were kept in the dark to avoid development of phototroph organisms.

Characterization

N_2 sorption analysis was performed at 77 K using a Micromeritics Tristar 3000, equipped with automated surface area and pore size analyzer. Before analysis, samples were degassed at 250 °C for 7 h using a Micromeritics VacPrep 061 degasser. Mercury intrusion porosimetry was performed using a Carlos Erba porosimeter. The initial measurement was performed using a Pascal 140 porosimeter at low pressure (400 kPa) followed by secondary analysis using a Pascal 240 porosimeter at high pressure (200 MPa). Pore diameters, D, were determined using the capillary law governing non-wetting liquid penetration into small pores expressed by the Washburn equation (1):

$$D = -4\,\gamma \,.\, \cos\varphi \,.\, (1/P_{Hg}) \qquad (1)$$

With:

- the surface tension of mercury $\gamma = 0.48$ N.m^{-1}
- and the contact angle $\varphi = 140°$

In this equation we assume that all pores are cylindrical.

Scanning electron microscope (SEM) images were obtained using a Gemini SEM (Figure 2a), a Hitachi SU3500 SEM with an Ultra-Variable Pressure Detector (Figure 6a), and a XL30 Philips (LaB6 source electron gun) SEM (Figures 6 b and c). Biofilm covered samples were rinsed in distilled water and let to dry before imaging.

High-resolution X-ray tomography was performed at the high-resolution setup MEDUSA of the Ghent University Centre for X-ray Tomography (UGCT). This system uses a FeinFocus FXE160.51 transmission tube with changeable target and a Photonic Science VHR camera with thin scintillator for a low energy response. The tomographic reconstruction is performed using Octopus Reconstruction (Inside Matters, Aalst, Belgium). A region of a large sample of approximately 4x7x15 mm^3 was scanned at a voxel size of 6^3 μm^3, whereas a small subsample of approximately 2x2x4 mm^3 was scanned at a voxel size of 1.6^3 μm^3. All datasets were reconstructed using the Modified Bronnikov Algorithm [62], as X-ray attenuation was negligible and phase contrast effects were visible. Furthermore, this algorithm offers a drastic improvement of signal-to-noise ratio [63].

Image analysis was performed on the small sample using Morpho+ [64], an in-house developed 3D analysis software tool. This package allows for a very modular analysis workflow, extensive parametrization of the pores and exporting of the analysed volume. The original gray scale volume was afterwards rendered together with the pore-size analysis data using Volume Graphics VGStudioMax.

Results

The as-synthesized carbonaceous material, 750-HMF-CarboHIPE, is mainly microporous (pores diameters inferior to 2 nm) as shown by the type I nitrogen sorption isotherm (Figure 1). High BET surface area and total pore volume of 1100 $m^2.g^{-1}$ and 0.52 $cm^3.g^{-1}$ respectively were determined. A slight hysteresis can be also seen, related to a little mesoporous contribution (pores diameters from 2 to 50 nm). At the macroscopic scale, a typical structure of aggregated hollow spheres, usually called *cells*, can be observed by scanning electron microscopy (SEM; Figure 2a). It corresponds to the removed soft template itself, *i.e.* the oil droplets of a direct emulsion. Herein, *cells* with diameters from 10 to 50 µm were obtained. Thus, the as-synthesized material can be seen as a foam, usually defined as microcellular. In addition to these *cells*, narrower pores could be observed by scanning electron microscopy at higher magnification (Figure 2a, insert). It can be assumed that these pores, usually called *connecting windows*, were induced either by the nonpolymerized interstices that remained in the continuous phase of the emulsion or by direct contacts between two nearby packed oil

droplets. As shown by SEM (Figure 2a), such windows have got diameters below 10 µm, with a broad size distribution centred at 1 µm. This feature was supported by mercury intrusion porosimetry (Figure 2b), showing a main contribution at 1 µm and few minor contributions from 10 nm up to 10 µm (Figure 2b-c).

The X-ray tomography analysis is a great addition to the SEM and mercury porosimetry analyses. To the best of our knowledge, X-ray tomography had never been applied to the characterization of carboHIPEs. All these techniques bring together a full picture of the bear materials as it had never been shown before. Due to the limitation of spatial resolution, the 3D analysis of the micro-CT dataset is limited to pores larger than several micrometer diameter. Furthermore, the absolute values of the results are prone to variations based on the thresholding step which is performed on the gray values. Nevertheless, 3D analysis gives extremely valuable information about the spatial distribution of the pore size distribution throughout the sample [65], where particularly the bigger pores contribute largely to the heterogeneity of a material. Additionally, the partial volume effect allows for the retrieval of information beyond the limits of the spatial resolution. Indeed, in a homogeneous but porous material, the local X-ray attenuation coefficient is directly proportional to the volume fraction of material in that area, where the area is defined by the spatial resolution of the dataset.

Figure 3 shows a combined rendering of the grayscale data with 3D analysis results. From the 3D analysis, no unpredicted properties can be found. The pores are randomly distributed in the volume, with their size normally distributed. The pores are mostly spherical, and consequently no preferential orientation of the pores can be observed. The pores are classified and color-coded according to their equivalent diameter, which is the diameter of the sphere with the volume of the pore and as such a linearized scale for pore volume. The gray scale represents the local density in the voxel. High-density regions at the outer edge are caused by sample handling and mounting; inside the sample the gray value variation is due to variation in smaller pores (< 1 µm) and image noise. In Figure 3a, the high-resolution scan is shown, giving information about pores of 2 microns and larger. Figure 3b shows the low-resolution scan, resolving only the pores larger than 10 µm equivalent diameter. The high resolution scan shows the widespread and large abundance of the smaller pores, with diameters from 2 to 10 µm, in agreement with the pore size distribution obtained by Hg-intrusion porosimetry (Figure

2b-c). Conversely, the low-resolution scan helps to visualize the distribution of the larger pores, which are not as abundant as the smaller ones. The occurrence of larger pores is somewhat hidden in Figure 3a. ~~In Figure 3b, a layered structure can be observed, indicating the macro-porous structure is not perfectly homogeneous on the macroscale (millimeter range)~~. The 3D scans confirm that a rather large pore size distribution is present in this sample, as already observed by the mercury intrusion porosimetry (see Figure 2), and that pores are spatially well distributed inside the sample. The extremely low X-ray attenuation of this sample also points out the high porosity of this sample, as shown by N_2 sorption data for micro- (below 2 nm) and mesopores (from 2 to 50 nm), although the size of such pores cannot be quantitatively confirmed by X-ray tomography.

Besides a fully interconnected macroporous network, the carbonaceous foam reported herein presented mechanical properties good enough to enable carefree handling and shaping (see ESI). After mercury intrusion porosimetry measurements, the materials used were still monolithic without showing any cracks. The monolithic foam was easily integrated in a membraneless home-made electrochemical reactor as depicted in Figure S1. Interestingly, the inoculation and bioelectrochemical experiments could be performed in a continuous flow through the as-designed microcellular carbonaceous reactor. The electrode managed to withstand undamaged the constant pressure exerted by the continuous flow. Finally, the bear material showed a reasonable electrical conductivity of 10 S m^{-1}.

Figure 4 shows the catalytic current development from time of inoculation with anodic effluent from an existing BES reactor. Catalytic current started to develop after 10 days. After 17 days, the current appeared to have reached a stationary value of 0.55 mA cm^{-2}. During 10 days the current remained at approximately constant values, within the expected fluctuations for a microbiological system. Afterwards the flow rate was increased from 0.033 ml min^{-1} to 0.115 ml min^{-1}, and a rather sharp current increase followed, with the current reaching 1.0 mA cm^{-2} . The flow rate was varied three more times to generate the current vs. flow rate graph that is shown in the inset of Figure 4. The flow rate was maintained at 0.214 ml min^{-1} from day 57 until day 94, when it was further decreased for the remaining of the experiment to 0.115 ml min^{-1}. The catalytic current reached a maximum value of 1.56 mA cm^{-2} (normalization by projected surface area). When normalized in current per volume unit of electrode, this value translates to 7.8 mA cm^{-3} at the highest flow rate. Attemps to test higher flow

rates were aborted because of repetitive issues with leakages and tubing problems when attempting to do so. Indeed Figure 4 still shows some sharp current decreases which were also due these experimental issues. An improved reactor design, would probably help reaching higher flow rates, which might help develop higher catalytic currents, and possibly also overcome pore clogging (see below).

Figure 5 (full line) shows the CV in turnover conditions. The voltammogram exhibits the classic sigmoidal shape of electroactive biofilms under turnover conditions with some degree of hysteresis. The current starts to increase above -0.45 V and reaches a plateau of maximum current around -0.15 V. The plateau current is almost the same as the maximum current recorded in the chronoamperometry experiment at the same flow rate. A first derivative analysis (shown in Figure S2 in Supporting Information) shows a symmetrical peak centred at -0.31 V (E_{hw}). The plateau current suggests that the maximum current is limited by either the enzymatic activity of acetate degradation, or diffusional limitations inside the three-dimensional electrode, i.e. arrival of acetate and diffusion of H^+ outside of the biofilm, and not by the interfacial kinetics of electron transfer. The onset potential for the start of the catalytic sigmoidal signal is governed by the redox potential of the redox moieties (be it soluble shuttles, membrane proteins or nanowires) interacting directly with the electrode surface. The wave shape and the onset potential are clear evidence of the microbial nature of the catalytic current, as has already been reported.[17, 41, 42, 59] Moreover, the blank experiments, before microbial inoculation showed almost nil current for the steady state chronoamperometry and no clear signal of faradaic reactions in the CV (see dashed line CV in Figure 5). The onset potential for the turnover CV and the value of E_{hw}, together with the strong red colour of our electrodes, see below, suggest that cytochromes are involved in the electron transfer from bacteria to electrode, although the detailed study of the electron transfer mechanism and the composition of the bacterial community are beyond the scope of this work.

At the end of the chronoamperometry experiment, the media in the reactor was replaced with fresh media without acetate. After 36h of an applied potential in the absence of substrate, cyclic voltammogram experiments were recorded in non-turnover conditions and are shown by the dotted line in Figure 5. The dashed curve shows for comparison the CV in abiotic conditions (before

inoculation). No clear peaks or seemingly faradaic processes are seen in either the abiotic or the non-turnover CV. Peaks in the non-turnover CV usually reveal the approximate redox potential of the species responsible for transferring electrons from the cells to the electrode. The apparent absence of these signals can be explained by the high non-faradaic currents which are characteristic of porous electrodes. Non-turnover peaks are usually of much lower magnitude than turnover signals and in data presented here they are most probably hidden under the high capacitive currents.

At the end of the chronoamperometry experiment, and upon opening the reactors, the electrodes showed a reddish colour on the upper surface, clearly distinctive to the naked eye. This is attributed to uniform biofilm coverage and suggests the presence of cytochromes. Figure 6 show SEM images of the biofilm developed in the inside and outside of the three-dimensional scaffold. Figure 6a shows a lateral view of the inside of the electrode (plane perpendicular to the cylinder base). We can observe a very thick biofilm coverage that has penetrated approximately the upper half of the cylinder (the image was taken close to the centre of the 2mm thick electrode). Surprisingly, the profile of biofilm coverage stops quite abruptly and below a certain height, there is no evidence of biological activity. The biofilm is dense and thick, and it seems to block many of the pores. This porosity blockage is most probably at the origin of the partial coverage of the interior of the electrode. We hypothesise that the biofilm started to develop in the upper surface of the electrode and developed both towards the inside and the outside of the scaffold. Figure 6b is a top view of the upper surface of the electrode. On the left side of the image, a thick and rough biofilm surface is distinguished, while on the right side, salt deposits partially cover the underlying biofilm (probably due to incomplete washing). Figures 6a and 6b together are proof of the generation of a thick and continuous biofilm in the whole upper surface and in the upper half of the interior of the monolith. Figure 6c is a zoom image on the exposed biofilm area seen in Figure 6b, where several individual microbial shapes can be distinguished. These appear to be rod-shaped and approximately 1 μm long.

Discussion

Interestingly, the 3D structure of our monolithic material was thoroughly characterized combining nitrogen sorption, mercury porosimetry and X-ray tomography. As for X-ray tomography, gathering experimental data was not easy, seeing that our samples are made almost exclusively from C, with smaller contributions of O and H, *i.e.* all very light elements with very small X-ray attenuation. Moreover, this sample displayed a hierarchical porosity. Thus, this foam was shown to be both highly macroporous – with total pore volume and porosity determined by Hg porosimetry of 9 $cm^3.g^{-1}$ and more than 95% respectively - and micro- mesoporous – with BET surface area and total pore volume of 1100 $m^2.g^{-1}$ and 0.52 $cm^3.g^{-1}$ respectively. Data shown in figure 3 were only made available thanks to the accuracy of an in-house built setup which is non-commercially available. This is the first time that the spherical shape of the macroscopic pores (cells) of carboHIPEs is experimentally observed. The 3D analysis also confirms the random distribution of pores sizes and occurrence along the whole volume of the material. Analysis of the X-ray tomography data indicates a macroporosity of only 20% (including macropores bigger than 2 µm only), whereas Hg porosimetry indicated a porosity value of more than 95 % (including pores from 10 nm to 100 µm). These features suggest a large contribution of smaller pores, *i.e.* smaller than 2 µm, confirmed by low X-ray attenuation and nitrogen sorption data. All in all, all the data gathered here indicate the excellent complementarity of the different techniques (SEM, N_2 sorption, Hg-intrusion and X-ray tomography) used here to fully characterize the porosity of these samples.

It is very important to note that the catalytic current was stable for 5 months of continuous operation. After 5 months the reactor was stopped and the electrode was taken out for SEM analyses, *i.e.* most probably the reactor could have remained operational for longer periods. This stability points out once more towards the high biocompatibility of the new material. Even though pore clogging was evident, this fact did not affect continuous operation of the reactor.

The catalytic current values achieved are below several recent reports on new advanced materials for microbial anodes.[17, 34, 41, 45] Today, the highest reported currents were achieved with extended macroporosity of 300µm[17] and 1.4mm.[34] A large quantity of macropores these sizes seem to be necessary to guarantee efficient mass transport of substrate towards the cells, and particularly to avoid

accumulation of H^+ and local pH changes.[17, 52, 66] The macroporosity of our new material is below these values, with pores sizes on average extending up to 50 µm, and very few pores with diameters larger than 150 µm (Figures 2 and 3). In the case of a highly biocompatible material, such as the one we are analyzing, another current limiting factor at this low pore size is pore clogging, due to bacteria overgrowth. We believe that the current densities achieved are a consequence of the reduce pore sizes. Nevertheless, we are confident that larger porosity while following a similar synthetic route will yield higher catalytic currents. Our data shows the high biocompatibility of the new materials as well as the long term activity of the microbial communities within the scaffolds.

The micro and mesopores of the 750-HMF-CarboHIPE are too small to contribute either to an increased available surface area for bacterial development or for improved liquid phase penetration inside the scaffold. However, we do believe that the nanometric features largely contributed to the high biocompatibility of this new material, providing a rough surface for bacterial attachment and connectivity for electron transfer.

Conclusions

We have presented a new carbonaceous material which is fully biocompatible and a good candidate to be incorporated into microbial bioelectrochemical systems. Our new material was synthesized from biomass derived precursors, making an interesting sustainable cycle: biomass is used for the synthesis of electrodes where a biofilm can develop that will oxidize organic matter present in wastewater.

We have proved the high biocompatibility of these new materials, with extended and continuous biofilm coverage both inside and outside the scaffold structure. The bacteria are electrically connected to the electrode surface, effectively transferring electrons to the electrode surface from the oxidation of organic matter.

Although the pore size distribution needs to be improved, these scaffolds are very promising as electrode materials for microbial bioelectrochemical systems. We are confident that an enlarged porosity will boost the current density, which so far is below other reported materials.

Acknowledgments

VF acknowledges a UQ Postdoctoral Fellowship. This work was supported by the Australian Research Council Grant DP110100539. The authors acknowledge the facilities and the scientific and technical assistance of the Australian Microscopy & Microanalysis Research Facility at the Centre for Microscopy and Microanalysis (The University of Queensland). The Ghent University Special Research Fund (BOF) is acknowledged for the post-doctoral grant of MNB.

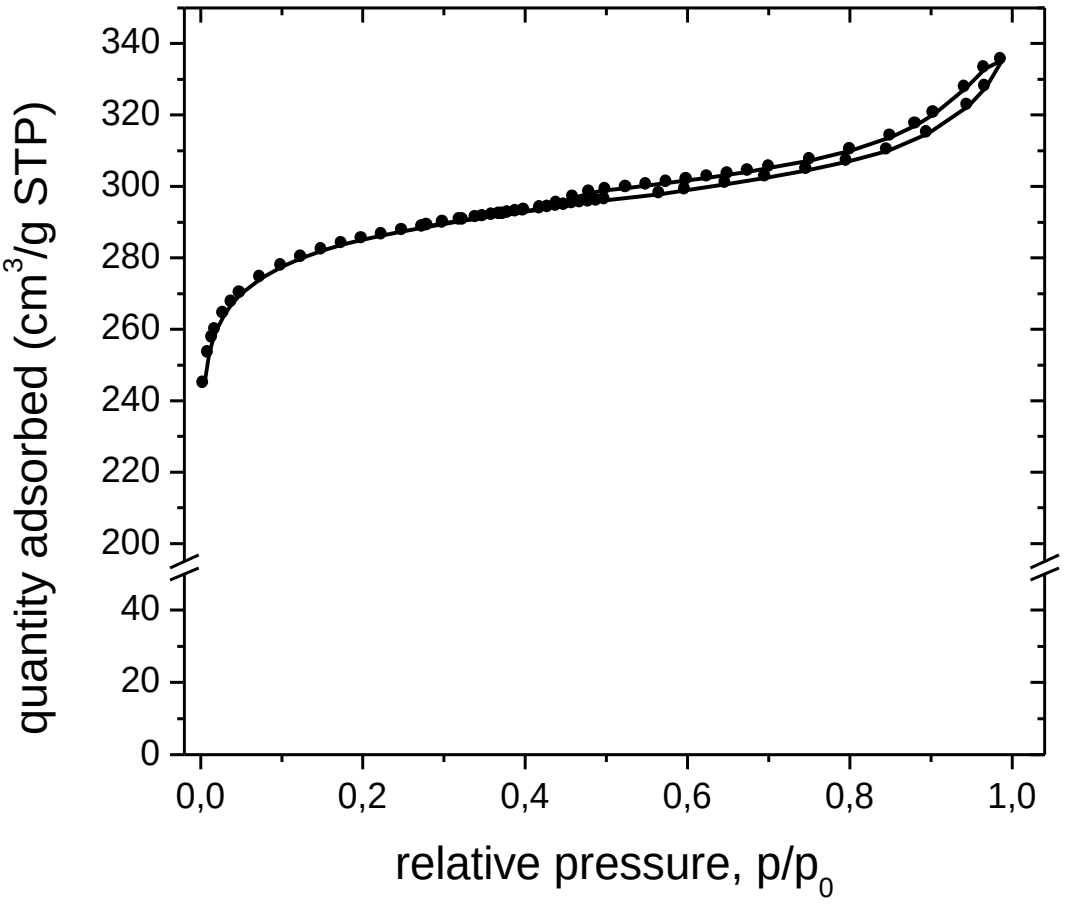

Figure 1: Nitrogen sorption isotherm of the unmodified carbonaceous foam, 750-HMF-CarboHIPE.

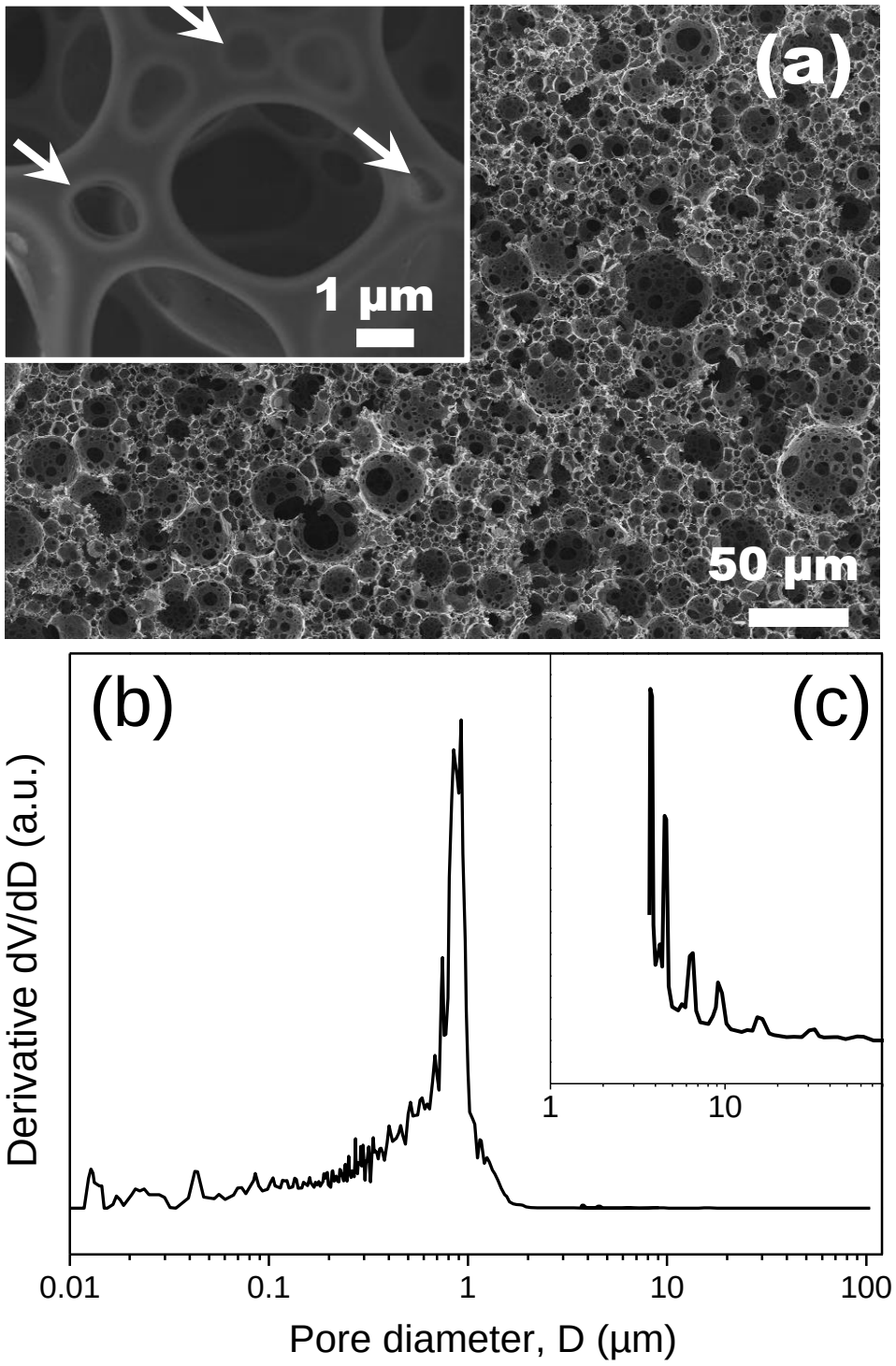

Figure 2: (a) SEM micrographs of the unmodified carbonaceous foam. The white arrows highlight the so-called connecting windows between macroscopic *cells*. (b) Macroscopic pore size distribution obtained by mercury intrusion porosimetry combining measurements performed using a Pascal 240 (up to 200 MPa) and a Pascal 140 (up to 400 KPa). (c) Data obtained at low pressure using a Pascal 140.

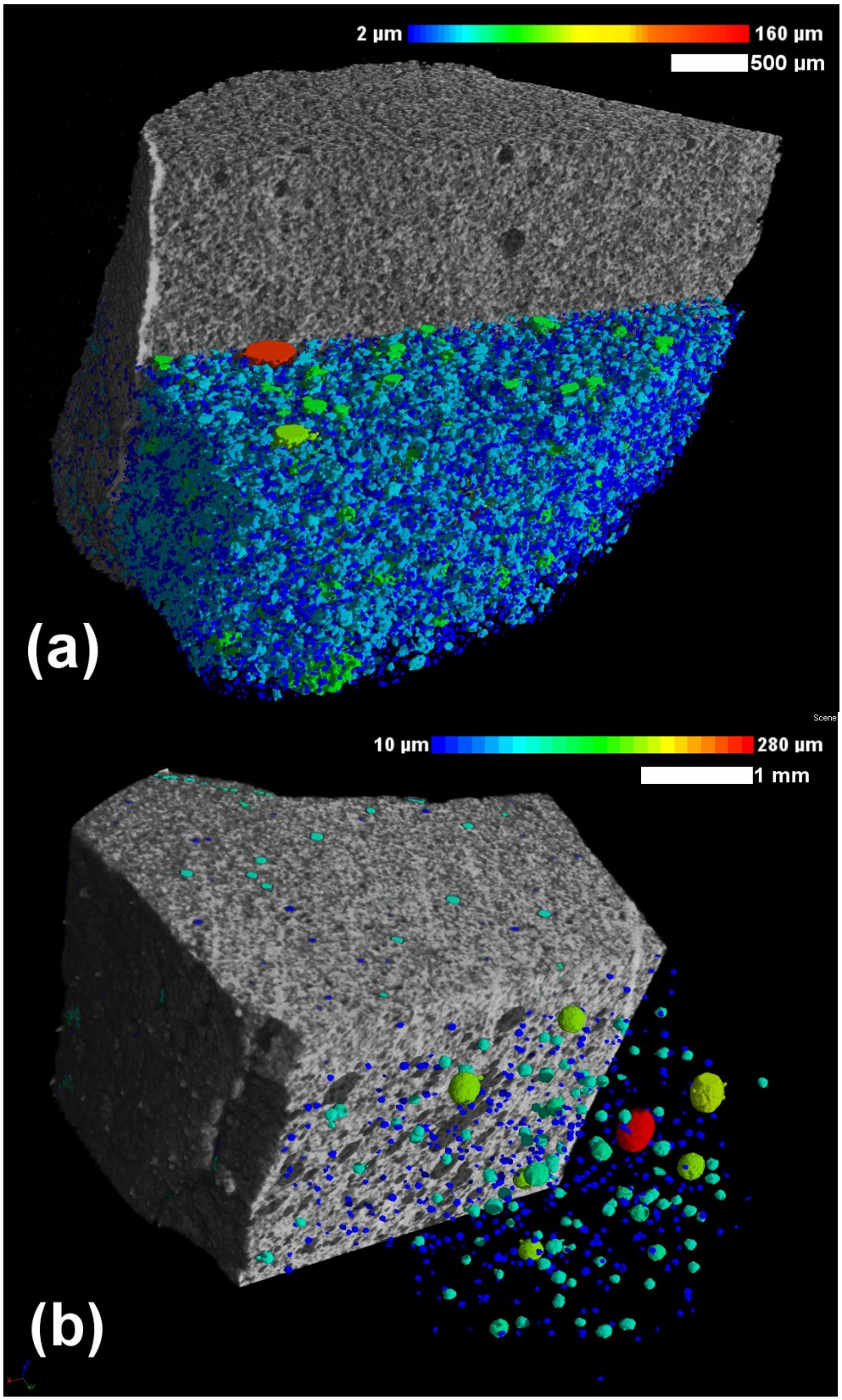

Figure 3: 3D renderings of the micro-CT scans, showing both the structure and the pore size analysis. Both volumes have been partially cut to improve visibility. The pores are color coded according to their equivalent diameter. (a) high-resolition scan; (b) low-resolution scan.

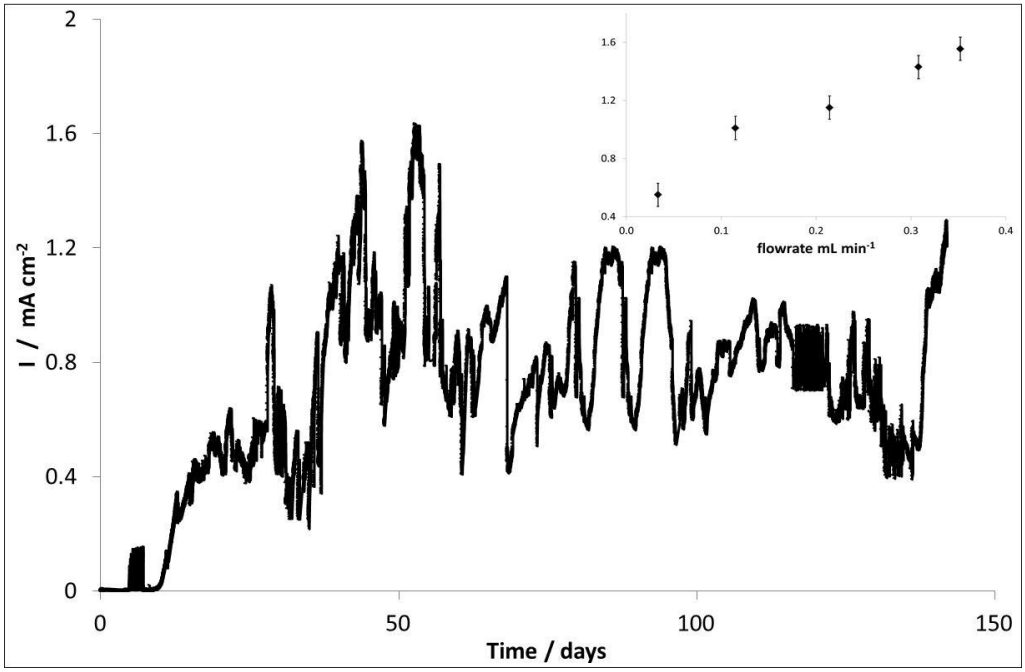

Figure 4: Bioelectrocatalytic current generation at a 750-HMF-CarboHIPE electrode in a continuous feed experiment. Biofilm derived from an anodic effluent and grown in artificial wastewater with 20 mM acetate, and applied electrode potential of 0 V (vs. Ag/AgCl). Varying flow rate as specified in the text. Inset: catalytic current vs. flow rate.

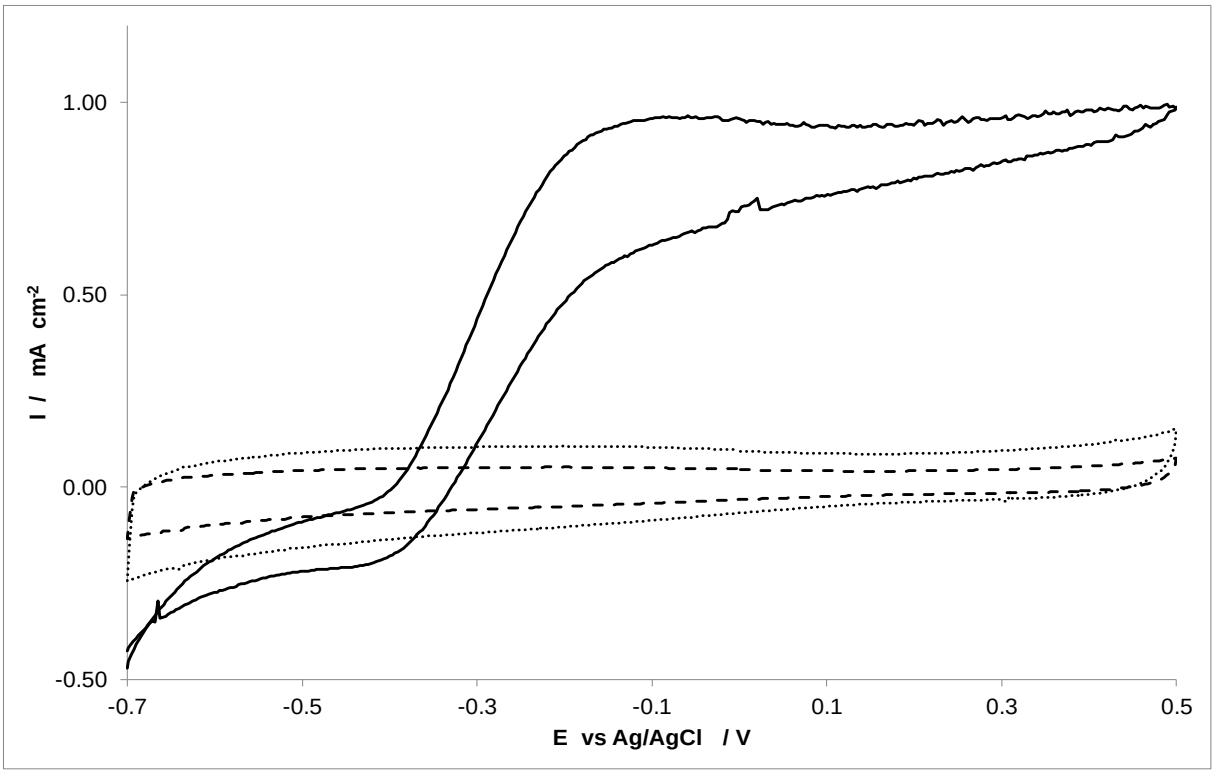

Figure 5: Cyclic voltammograms recorded at 0.1 mV s^{-1}, and in media as described in the experimental section. Dashed line: before inoculation, in presence of 20mM acetate. Full line: after 54 days of inoculation, in the presence of 20 mM acetate. Dotted line: after 190 days of inoculation, no acetate.

Figure 6: SEM micrographs after biofilm development. Top: Side view (inverted image, bottom of the image is actually the top of the electrode in Figure S1). Middle and Bottom: top of the electrode at different magnification.

References

[1] E. Frackowiak, F. Beguin, Carbon, 39 (2001) 937-950.
[2] S.L. Candelaria, Shao, Y., Zhou, W., Li, X., Xiao, J., Zhang, J.-G., Wang, Y., Liu, J., Li, J., Cao, G., Nano Energy, 1 (2012) 195-220.
[3] J. Biener, M. Stadermann, M. Suss, M. Worsley, M. Biener, K. Rose, T. Baumann, Energy & Environmental Science, 4 (2011) 656-667.
[4] V. Flexer, N. Brun, R. Backov, N. Mano, Energy and Environmental Science, 3 (2010) 1302-1306.
[5] J.L. Figueiredo, Journal of Materials Chemistry a, 1 (2013) 9351-9364.
[6] Z. Wu, C. Li, H. Liang, J. Chen, S. Yu, Angewandte Chemie-International Edition, 52 (2013) 2925-2929.
[7] C. Zhang, W. Tjiu, T. Liu, Rsc Advances, 3 (2013) 14938-14941.
[8] M. Sevilla, A. Fuertes, Energy & Environmental Science, 4 (2011) 1765-1771.
[9] M. Sevilla, A. Fuertes, R. Mokaya, Energy & Environmental Science, 4 (2011) 1400-1410.
[10] C. Falco, J. Sieben, N. Brun, M. Sevilla, T. van der Mauelen, E. Morallon, D. Cazorla-Amoros, M. Titirici, Chemsuschem, 6 (2013) 374-382.
[11] K. Tang, L. Fu, R. White, L. Yu, M. Titirici, M. Antonietti, J. Maier, Advanced Energy Materials, 2 (2012) 873-877.
[12] K. Tang, R. White, X. Mu, M. Titirici, P. van Aken, J. Maier, Chemsuschem, 5 (2012) 400-403.
[13] L. Wang, Z. Schnepp, M. Titirici, Journal of Materials Chemistry a, 1 (2013) 5269-5273.
[14] M. Soorholtz, R. White, T. Zimmermann, M. Titirici, M. Antonietti, R. Palkovits, F. Schuth, Chemical Communications, 49 (2013) 240-242.
[15] V. Flexer, N. Brun, O. Courjean, R. Backov, N. Mano, Energy and Environmental Science, 4 (2011) 2097-2106.
[16] V. Flexer, N. Brun, M. Destribats, R. Backov, N. Mano, Physical Chemistry Chemical Physics, 15 (2013) 6437-6445.
[17] V. Flexer, J. Chen, B.C. Donose, P. Sherrell, G.G. Wallace, J. Keller, Energy and Environmental Science, 6 (2013) 1291-1298.
[18] N. Brun, L. Edembe, S. Gounel, N. Mano, M.M. Titirici, ChemSusChem, 6 (2013) 701-710.
[19] W. Yang, T. Fellinger, M. Antonietti, Journal of the American Chemical Society, 133 (2011) 206-209.
[20] S. Wohlgemuth, T. Fellinger, P. Jaker, M. Antonietti, Journal of Materials Chemistry a, 1 (2013) 4002-4009.
[21] N. Brun, S.A. Wohlgemuth, P. Osiceanu, M.M. Titirici, Green Chemistry, ***15*** (2013) 2514-2524.
[22] N. Brun, P. Osiceanu, M.M. Titirici, ChemSusChem, 7 (2014) 397-401.
[23] N. Brun, S. Ungureanu, H. Deleuze, R. Backov, Chemical Society Reviews, 40 (2011) 771-788.
[24] Bioelectrochemical Systems: From Extracellular Electron Trnasfer to Biotechnological Applications, IWA Publishing, London, 2010.
[25] B.E. Logan, Nature Reviews Microbiology, 7 (2009) 375-381.
[26] D.R. Lovley, Nature Reviews Microbiology, 4 (2006) 497-508.
[27] K. Rabaey, W. Verstraete, Trends in Biotechnology, 23 (2005) 291-298.
[28] L. Jourdin, S. Freguia, B. C. Donose, J. Chen, G. G. Wallace, J. Keller and V. Flexer, *Journal of Materials Chemistry A*, 2014, **2**, 13093-13102..
[29] L. Jourdin, S. Freguia, B. C. Donose and J. Keller, *Bioelectrochemistry*, 2015, **102**, 56-63.
[30] L. Jourdin, T. Grieger, J. Monetti, V. Flexer, S. Freguia, Y. Lu, J. Chen, M. Romano, G. G. Wallace and J. Keller, *Environmental Science & Technology*, 2015, **49**, 13566-13574.
[31] K. Rabaey, R.A. Rozendal, Nature Reviews Microbiology, 8 (2010) 706-716.
[32] S. A. Patil, J. B. A. Arends, I. Vanwonterghem, J. van Meerbergen, K. Guo, G. W. Tyson, and K. Rabaey, *Environmental Science and Technology*, 2015, **49**, 8833-8843.
[33] P.L. Tremblay and T. Zhang, *Frontiers in Microbiology*, 2015, **6**, 201.
[34] S. Chen, G. He, Q. Liu, F. Harnisch, Y. Zhou, Y. Chen, H. Muddasir, S. Wang, X. Peng, H. Hou, U. Schroeder, Energy & Environmental Science, 5 (2012) 9769-9772.
[35] B.E. Logan, Applied Microbiology and Biotechnology, 85 (2010) 1665-1671.
[36] R.A. Rozendal, H.V.M. Hamelers, K. Rabaey, J. Keller, C.J.N. Buisman, Trends in Biotechnology, 26 (2008) 450-459.

[37] T. Krieg, A. Sydow, U. Schröder, J. Schrader, D. Holtmann, *Trends in Biotechnology*, 2014. **32**, 645-655.
[38] F. Harnisch, L. F. M. Rosa, F. Kracke, B. Virdis, J. O. Krömer, *ChemSusChem*, 2015, **8**, 758-766.
[39] M. Zhou, M. Chi, J. Luo, H. He, T. Jin, Journal of Power Sources, 196 (2011) 4427-4435.
[40] J. Wei, P. Liang, X. Huang, Bioresource Technology, 102 (2011) 9335-9344.
[41] S. Chen, H. Hou, F. Harnisch, S.A. Patil, A.A. Carmona-Martinez, S. Agarwal, Y. Zhang, S. Sinha-Ray, A.L. Yarin, A. Greiner, U. Schroder, Energy & Environmental Science, 4 (2011) 1417-1421.
[42] S. Chen, Q. Liu, G. He, Y. Zhou, M. Hanif, X. Peng, S. Wang, H. Hou, Journal of Materials Chemistry, 22 (2012) 18609-18613.
[43] X. Xie, M. Ye, L. Hu, N. Liu, J.R. McDonough, W. Chen, H.N. Alshareef, C.S. Criddle, Y. Cui, Energy & Environmental Science, 5 (2012) 5265-5270.
[44] S.R. Higgins, D. Foerster, A. Cheung, C. Lau, O. Bretschger, S.D. Minteer, K. Nealson, P. Atanassov, M.J. Cooney, Enzyme and Microbial Technology, 48 (2011) 458-465.
[45] K. Katuri, M.L. Ferrer, M.C. Gutiérrez, R. Jiménez, F. Del Monte, D. Leech, Energy and Environmental Science, 4 (2011) 4201-4210.
[46] J.E. Mink, J.P. Rojas, B.E. Logan, M.M. Hussain, Nano Letters, 12 (2012) 791-795.
[47] X. Xie, L. Hu, M. Pasta, G.F. Wells, D. Kong, C.S. Criddle, Y. Cui, Nano Letters, 11 (2011) 291-296.
[48] S. Chen, G. He, X. Hu, M. Xie, S. Wang, D. Zeng, H. Hou, U. Schröder, ChemSusChem, 5 (2012) 1059-1063.
[49] S. Chen, G. He, A.A. Carmona-Martinez, S. Agarwal, A. Greiner, H. Hou, U. Schröder, Electrochemistry Communications, 13 (2011) 1026-1029.
[50] Y. Zhao, K. Watanabe, R. Nakamura, S. Mori, H. Liu, K. Ishii, K. Hashimoto, Chemistry - A European Journal, 16 (2010) 4982-4985.
[51] E. Kipf, J. Koch, B. Geiger, J. Erben, K. Richter, J. Gescher, R. Zengerle, S. Kerzenmacher, Bioresource Technology, 146 (2013) 386-392.
[52] Y. Yuan, S. Zhou, Y. Liu, J. Tang, Environmental Science and Technology, 47 (2013) 14525-14532.
[53] S.A. Patil, S. Chigome, C. Hägerhäll, N. Torto, L. Gorton, Bioresource Technology, 132 (2013) 121-126.
[54] Y.C. Yong, X.C. Dong, M.B. Chan-Park, H. Song, P. Chen, ACS Nano, 6 (2012) 2394-2400.
[55] T. Zhang, H. Nie, T.S. Bain, H. Lu, M. Cui, O.L. Snoeyenbos-West, A.E. Franks, K.P. Nevin, T.P. Russell, D.R. Lovley, Energy and Environmental Science, 6 (2013) 217-224.
[56] T. Huggins, H. Wang, J. Kearns, P. Jenkins, Z.J. Ren, Bioresource Technology, 157 (2014) 114-119.
[57] K. Guo, A. Prévoteau, S. A. Patil, K. Rabaey, Current Opinion in Biotechnology, 33 (2015) 149-156.
[58] K. Guo, S. Freguia, P.G. Dennis, X. Chen, B.C. Donose, J. Keller, J.J. Gooding, K. Rabaey, Environmental Science and Technology, 47 (2013) 7563-7570.
[59] V. Flexer, M. Marque, B.C. Donose, B. Virdis, J. Keller, Electrochimica Acta, 108 (2013) 566-574.
[60] P.G. Dennis, K. Guo, M. Imelfort, P. Jensen, G.W. Tyson, K. Rabaey, Bioresource Technology, 129 (2013) 599-605.
[61] K. Rabaey, W. Ossieur, M. Verhaege, W. Verstraete, Water Science and Technology, 52 (2005) 515-523.
[62] Groso, A., et al., Optics Express, 2006. **14**(18): 8103-8110
[63] Boone, M.N., et al., Microscopy and Microanalysis, 2012. **18**(2): 399-405.
[64] Brabant, L., et al., Microscopy and Microanalysis, 2011. **17**(2): 252-263.
[65] Almeida, A., et al., European Journal of Pharmaceutics and Biopharmaceutics, 2011. **77**(2): 297-305.
[66] C.I. Torres, A.K. Marcus, B.E. Rittmann, Biotechnology and Bioengineering, 100 (2008) 872-881.